RSC Advances

PAPER

View Article Online
View Journal | View Issue

Cite this: *RSC Adv.*, 2021, **11**, 17352

A three-dimensional nanostructure of $NiFe(OH)_X$ nanoparticles/nickel foam as an efficient electrocatalyst for urea oxidation

Xue-Li Yang,†[a] Ya-Wen Lv,†[a] Jun Hu,†[a] Jing-Ru Zhao,[a] Guo-Yong Xu,[b] Xiao-Qiang Hao,[a] Ping Chen *[ab] and Man-Qing Yan*[a]

Received 16th February 2021
Accepted 1st April 2021

DOI: 10.1039/d1ra01276b

rsc.li/rsc-advances

Developing high-performance electrocatalysts for urea oxidation reaction (UOR) can not only solve the problem of environmental pollution, but also solve the problem of the energy crisis by producing hydrogen for electrodes. The preparation of porous three-dimensional nanostructures as efficient electrocatalysts has become important work. Here, we developed a novel three-dimensional (3D) nanostructure of $NiFe(OH)_X$ nanoparticles/nickel foam with a high active area by a simple electroplating method and a subsequent treatment with ferric ion solution. This structure shows much greater UOR activity than the control sample (Ni/Ni foam) with the potential of 1.395 V (*vs.* RHE) (with an overpotential of 1.025 V) for driving the current density of 100 mA cm^{-2} in 1.0 M KOH electrolyte with 0.33 M urea. This work not only provides rapid and large-scale preparation of a three-dimensional nanostructure, but also gives a new way to design and obtain high-performance electrocatalysts.

1. Introduction

With the rapid development of science and technology, it was bound to cause a large increase in energy demand (like coal, petroleum, and natural gas), at the same time, it would lead to the excessive use of non-renewable energy, resulting in the occurrence of energy depletion.[1] As a result, more effective and green energy storage and conversion technologies have emerged,[2] especially for the development and utilization of renewable clean energy (like tidal, solar, and wind energy).[3] Hydrogen energy was considered as one of the most promising and efficient energy sources,[4,5] which can replace the traditional fossil energy because of its higher energy density and zero pollution emission.[6] Generally speaking, the water electrolysis strategy is one of the most efficient ways to produce hydrogen energy, which is composed of the anodic oxygen evolution reaction (OER) and cathodic hydrogen evolution reaction (HER)[7–10] and is sought after and loved by many researchers.[11,12] However, as the most important half-reaction of the anode of water electrolysis, oxygen evolution reaction (OER) has sluggish kinetics and is complicated by a four-electron transferring process ($4OH^- \rightarrow 2H_2O + O_2 + 4e^-$), which seriously hinders the conversion and application of hydrogen energy process.[13] The urea oxidation reaction (UOR), which was also an anode reaction, has a 6-electron transmission process ($CO(NH_2)_2 + 6OH^- \rightarrow N_2 + 5H_2O + CO_2 + 6e^-$). It was considered to be a half-reaction for producing hydrogen energy, and can also provide a certain solution for sewage treatment owing to the urine in the human body contains a large amount of urea. The anodic electrocatalysis of urea oxidation can obtain a lower theoretical potential of 0.37 V than the electrocatalysis of water oxidation (1.23 V). In contrast, by changing the anode reaction urea oxidation reaction (UOR), the price of hydrogen energy can be effectively dropped.[8]

For well over the last few years now, transition metal hydroxides (nanoparticles) have been widely used in OER due to their excellent electrocatalytic properties in alkaline media. So far, many different types of nanoparticles have been synthesized, such as NiCo nanoparticles,[14–16] NiFe nanoparticles,[17–19] CoFe nanoparticles[20] and so on. Compared with the metal materials widely used in OER reaction, UOR mainly centers on nickel based materials, such as nickel-based oxide,[21–23] Ni alloys,[24,25] Ni-based hydroxides oxides,[26–28] sulfides and so on,[29–32] which is closely related to its principle. The main reason is that there are some active enzymes that decompose urea in the human body, and the active center is the nickel atom, which decomposes urea into carbon dioxide and water. Therefore, a series of nickel-based materials with catalytic activity have emerged.[33,34]

Generally, it was believed that the electrocatalytic reaction was a multi-step reaction involving adsorption and desorption, and the main products occurred on the surface of the catalyst materials by electron transfer.[35,36] Therefore, the design of functional materials with nano-porous structure can greatly

[a]*School of Chemistry and Chemical Engineering, Anhui University, Hefei, Anhui, 230601, P. R. China. E-mail: chenping@ahu.edu.cn; yanmanq@ahu.edu.cn*

[b]*Institute of Physical Science and Information Technology, Anhui University, Hefei, 230601, P. R. China*

† These authors have the equal contribution to this paper.

improve the catalytic activity.[37,38] Our group reported the novel 3D porous nanostructure (Co/Co_3O_4/C–N) of an interconnected nitrogen-doped carbon framework with Co/Co_3O_4 nanoparticles.[39] Xu *et al.* reported 3D porous nanomaterials electrocatalyst that can catalyze both UOR and HER by fabricating the *in situ* grown Ni phosphate (shell)-anchored $Ni_{12}P_5$ nanorod (core) arrays on the 3D Ni foam skeleton. So, the design of 3D porous nanomaterials based on nickel-based bimetal materials is of great practical significance and can better catalyze the decomposition of urea through the synergistic effect of bimetals.[40]

In this paper, we electroplated nickel on the surface of the nickel foam with a three-dimensional structure through a simple two-electrode electroplating method, thereby increasing the active area of the nickel foam. At the same time, using a mild chemical reaction, the interaction between ferric ions and nickel made a layer of composite hydroxide formed on the surface of the electroplated layer. In the end, the specific surface area of the overall structure of the material had been enlarged and providing a universal method. Therefore, the electrochemical performance had been greatly improved. Under the three-electrode system, the $NiFe(OH)_X$ nanoparticles/Ni foam sample yields much greater UOR activity than the control sample (Ni/Ni foam) with a lower potential of 1.395 V (*vs.* RHE) (with an overpotential of 1.025 V) for achieving 100 mA cm^{-2} in 1.0 M KOH electrolyte with 0.33 M urea. In this work, a rapid and large-scale preparation of three-dimensional nanostructure was developed and a new way to design and obtain high-performance electrocatalysts was proposed.

2. Experimental section

2.1 Chemical

Nickel chloride ($NiCl_2 \cdot 6H_2O$), ferric nitrate ($FeN_3O_9 \cdot 9H_2O$) and ammonium chloride (NH_4Cl) were purchased from Macklin Inc. All chemicals were used without any further purification. Nickel foam (thickness: 1.7 mm, 320 ± 25 g m^{-2}) was purchased from Heze Tianyu Technological Development Liability Co., Ltd. Nickel foam (3 cm × 3 cm) was ultrasonicated in 2.0 M HNO_3 for 10 min to remove the surface of oil and oxide layer, followed by rinsing with ethanol and deionization water for two times, and then vacuum-dried at 60 °C for 6 hours.

2.2 Synthesis of the Ni/Ni foam

The Ni/Ni foam was synthesized by two-electrode deposition using a CHI 660E electrochemical working station (Chenhua, China) with Ni foam as the substrate. In this typical synthesis, 5.449 g NH_4Cl and 2.3769 g $NiCl_2$ were dissolved in 100 mL H_2O to form a clear solution. Then electrochemical deposition was carried out by using platinum plate electrode as a counter electrode and Ni foam as a working electrode that working under the condition of current value of 2.5 A for 3 minutes. Then it can be clearly seen that a layer of black product was attached to the surface of the Ni foam. Finally, the covered foams were rinsing with ethanol and deionization water for three times, and then freeze-dried for 12 hours.

2.3 Synthesis of the $NiFe(OH)_X$ nanoparticles/Ni foam sample

In a typical preparation, 0.404 g $FeN_3O_9 \cdot 9H_2O$ was dissolved into 80 mL of deionization water and 20 mL of ethanol under stirring. The mixed aqueous solution was transferred into a 250 mL three-necked flask and heated at 60 °C in an oil bath for 2 hours. When the temperature of the oil bath reaches 60 °C, the prepared Ni/Ni foam was added to the three-necked flask over without stirring. After cooling down to room temperature, the $NiFe(OH)_X$ nanoparticles/Ni foam was washed with distilled water and ethanol for several times and then freeze-dried for 12 hours.

2.4 Characterization

The phase structure of products were characterized on a D8 advance X-ray diffraction (XRD) with Cu Kα radiation of wavelength (λ = 0.154 nm). The structure and morphology were investigated by a scanning electron microscopy (FEI NANOSEM 650/EDS) and a transmission electron microscopy (JEM 2100F STEM/HRTEM). The surface chemical states of the $NiFe(OH)_X$ nanoparticles/Ni foam were investigated by the X-ray photoelectron spectroscopy (XPS) on ESCALab MKII X-ray photoelectron spectrometer. The Raman spectra were carried out on a Renishaw Invia Raman spectrometer (wavelength = 532 nm).

2.5 Electrochemical measurement

All the electrochemical measurements were performed by an electrochemical working station (CHI 660E). The electrocatalytic performance of the Ni/Ni foam and the $NiFe(OH)_X$ nanoparticles/Ni foam were studied with the three-electrode system at the room temperature. The Ni/Ni foam and the $NiFe(OH)_X$ nanoparticles/Ni foam were used as the working electrode, respectively. A Hg/HgO (1.0 M KOH) electrode and a Pt electrode were used as the reference and the counter electrode, respectively. The linear sweep voltammetry (LSV) for UOR was tested according to the following equation: $E_{(RHE)} = E_{(Hg/HgO)} + 0.098\ V + 0.0591 \times pH$. Electrochemical impedance spectroscopy (ESI) was analyzed in a frequency range from 100 kHz to 0.01 Hz by applying an amplitude of 5 mV. All the curves were used with IR compensation. According to the following equations in two-electrode system, the faradaic efficiency of hydrogen can be evaluated: $F(H_2) = (m \times n \times F)/Q$, F is faradaic constant (F = 96 485 C mol^{-1}), m is the moles of product, n denotes transferred electrons and Q denotes the consumed charge. The electrocatalytic stability performance of the samples was studied by multi-current step and chronoamperometry measurement without *iR*-correction. In the two-electrode system, the $NiFe(OH)_X$ nanoparticles/Ni foam and Pt electrode were directly used as cathode and anode, respectively. The anion diaphragm-separated H-type reactor was used to test the performance of the electrode in the two-electrode mode. 80 mL KOH (1.0 M) + 0.33 M urea electrolyte was added to each compartment. The gas sample was delivered directly to the sampling loop of an on-line gas chromatograph. H_2 was detected by TDX-01 column with a thermal conductivity detector (TCD) using Ar as a carrier gas.

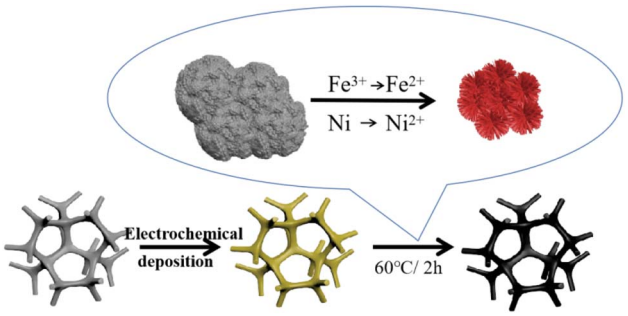

Scheme 1 Schematic illustration of the preparation of the $NiFe(OH)_X$ nanoparticles/Ni foam.

3. Results and discussion

The first step of the $NiFe(OH)_X$ nanoparticles/Ni foam sample synthesis was to reduce the metal ion nickel to elemental nickel through the two-electrode method and attached it to the surface of the foamed nickel with a three-dimensional structure. At the same time, the elemental nickel attached to the surface of the three-dimensional structure also had a certain hole effect, which not only increased the specific surface area of the overall structure of the material, but also facilitated the penetration of electrolyte ions and the oxidation of urea molecules. When the material was immersed in ferric ion solution, the surface of the material would react with ferric ion as follows:

$$2Fe^{3+} + Ni \rightarrow Ni^{2+} + 2Fe^{2+}$$

$$O_2 + 2H_2O + 4Fe^{2+} \rightarrow 4OH^- + 4Fe^{3+}$$

$$Ni^{2+} + Fe^{3+} + OH^- \rightarrow NiFe(OH)_X \text{ nanoparticles}$$

Finally, due to the gentle reaction between iron ions and elemental nickel, the nickel-based material with a three-dimensional nanostructure had a higher specific surface area and more active sites. At the same time, the immersion of iron ions also aggravated the progress of the catalytic reaction, making the catalytic activity for UOR was much higher than that on the original basis (Scheme 1).

Fig. 1 shows scanning electron microscopy images of the Ni/Ni foam (a and b) and the $NiFe(OH)_X$ nanoparticles/Ni foam (c and d) at different magnifications. From Fig. 1a and b, it can clearly see that nickel can be easily plated on the surface of nickel foam and form a coral like pore structure using the industrial electroplating method. When the trivalent iron ion was immersed (Fig. 1c and d), it first reacted with the nickel of the electrodeposited coating. At this time, the coral like structure gradually decreased with the continuous reaction, and the specific surface area gradually increased, which was conducive to the increase of the active sites of the whole material and the catalytic reaction. From Fig. 1b and d, it can clearly see the differences between the two before and after the reaction. The particle size of the original electroplating layer is about 1 μm. After the reaction, the particles become smaller and the size is about 200 nm. The fundamental reason is the immersion and reaction of ferric ions.

Transmission Electron Microscopy (TEM) images showed that, after trivalent iron ions are corroded, a series of mild reactions will occur on the surface of the original particles, resulting in the formation of a thin layer structure on the surface of the electroplated nickel. The diameter of the $NiFe(OH)_X$ nanoparticles is about 200 nm, just like the result of the SEM images in Fig. 1d. Fig. 2b showed the high-resolution

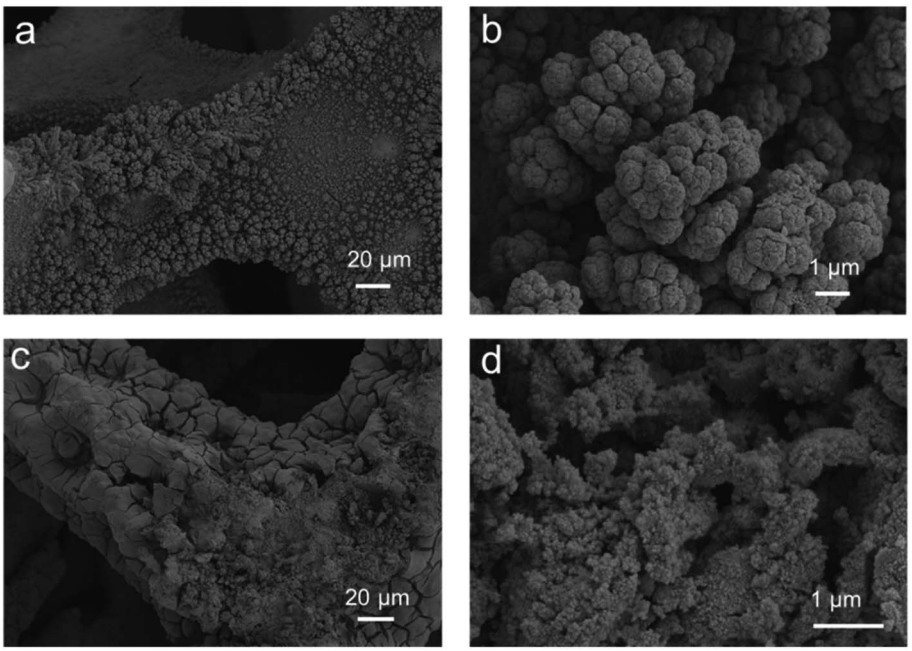

Fig. 1 SEM images of the Ni/Ni foam (a and b), the $NiFe(OH)_X$ Nanoparticles/Ni foam (c and d).

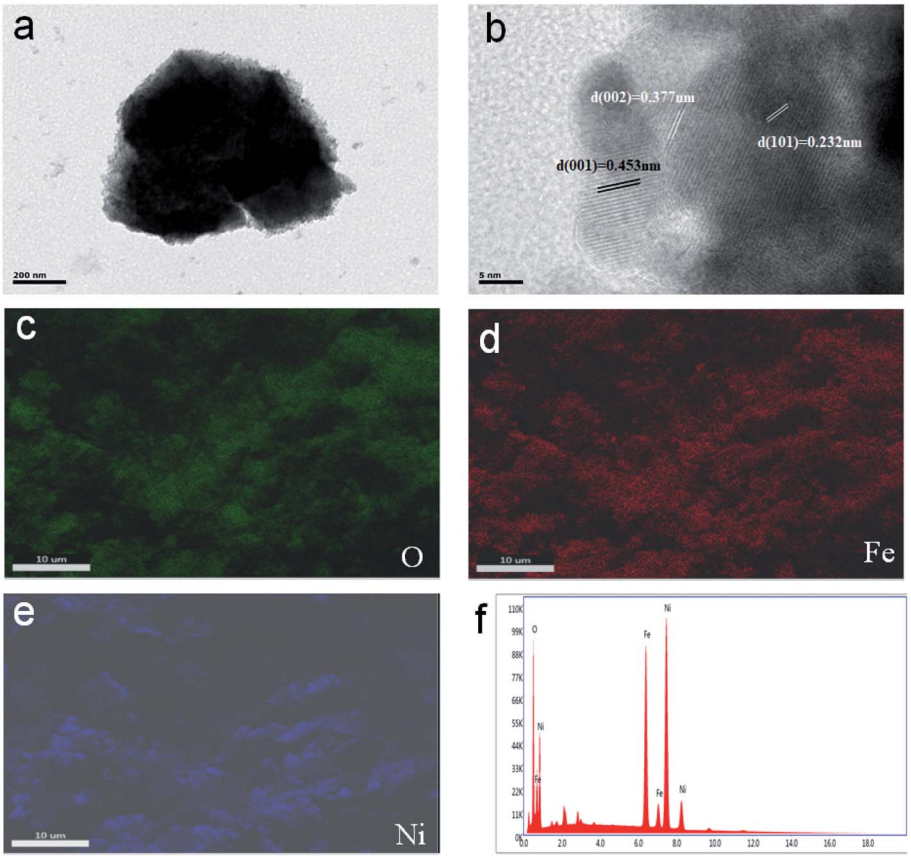

Fig. 2 (a) TEM and (b) HRTEM images of the $NiFe(OH)_X$ nanoparticles/Ni foam. The mapping images of (c) O, (d) Fe, (e) Ni and the energy-dispersive X-ray spectrometry spectra (f) of the $NiFe(OH)_X$ nanoparticles/Ni foam.

transmission electron microscopy images of the $NiFe(OH)_X$ nanoparticles. As the result showed that the visible lattice fringes separated by an interplanar distance of 0.453 nm and 0.232 nm can safely correspond to the (001) and (101) planes of $Ni(OH)_2$, respectively. This can prove that when ferric ions were immersed, the corresponding elemental nickel would be converted into divalent hydroxide. Meanwhile, the lattice fingers with the spacing of 0.377 nm in Fig. 2b correspond to the (002) plane of $Fe(OH)_3$. Furthermore, the energy-dispersive X-ray spectrometry spectra of the $NiFe(OH)_X$ nanoparticles/Ni foam with corresponding mapping images of O, Fe and Ni have homogeneously distributed over the $NiFe(OH)_X$ nanoparticles (Fig. 2c–f).

X-ray photoelectron spectroscopy (XPS) was measured to further investigate the chemical states and oxidation states of the $NiFe(OH)_X$ nanoparticles/Ni foam sample surface. The binding energy of 528.9 eV, 530.6 eV and 531.8 eV in the O 1s spectra (Fig. 3a) was representative of typical metal–oxygen bond, the oxygen in the hydroxide group and chemisorbed molecular, respectively. Obviously, the oxygen in the hydroxide group occupied the main part of the $NiFe(OH)_X$ nanoparticles/Ni foam sample surface. The binding energy of Ni 2p spectra from the $NiFe(OH)_X$ nanoparticles/Ni foam sample surface in Fig. 3b, consisting of two spin–orbit doublets of Ni $2p_{1/2}$ (874.6 eV) and Ni $2p_{3/2}$ (856.8 eV), that can be noted as $Ni(OH)_2$. Meanwhile, in the Fe 2p core level spectra (Fig. 3c), the Fe $2p_{1/2}$ and Fe $2P_{3/2}$ peaks centered at 725.0 eV and 712.4 eV can be attributed to $Fe(OH)_3$.[41] The Raman spectra of the $NiFe(OH)_X$ nanoparticles/Ni foam sample was confirmed, which the bands at around 480 cm^{-1} and 680 cm^{-1} can be assigned of Ni–O in disordered $Ni(OH)_2$. Meanwhile, the Raman bands at 224 cm^{-1}, 288 cm^{-1} and 1313 cm^{-1} was originated α-Fe_2O_3 clusters, that due to the dehydration caused by unstable $Fe(OH)_3$ under dry conditions.[42]

The catalytic activities of the $NiFe(OH)_X$ nanoparticles/Ni foam sample and the Ni/Ni foam were examined by a three-electrode system in 1.0 M KOH electrolyte with 0.33 M urea at a scan rate of 10 mV s^{-1}, respectively. In the system, a Hg/HgO electrode and a Pt electrode were used as the reference and the counter electrode, respectively. As observed in Fig. 4a, UOR occurred on the $NiFe(OH)_X$ nanoparticles/Ni foam sample in 1.0 M KOH electrolyte with 0.33 M urea at the potential of 1.332 V that a lower potential than the Ni/Ni foam (1.341 V) and the Ni foam (1.350 V). Additionally, the $NiFe(OH)_X$ nanoparticles/Ni foam sample yields much greater UOR activity than the Ni/Ni foam with a lower potential of 1.395 V (with an overpotential of 1.025 V) for achieving 100 mA cm^{-2} in 1.0 M KOH electrolyte with 0.33 M urea. Tafel plots were normally used to investigate the activity in the catalytic kinetic of UOR. As shown in Fig. 4b, the Tafel slope of the $NiFe(OH)_X$

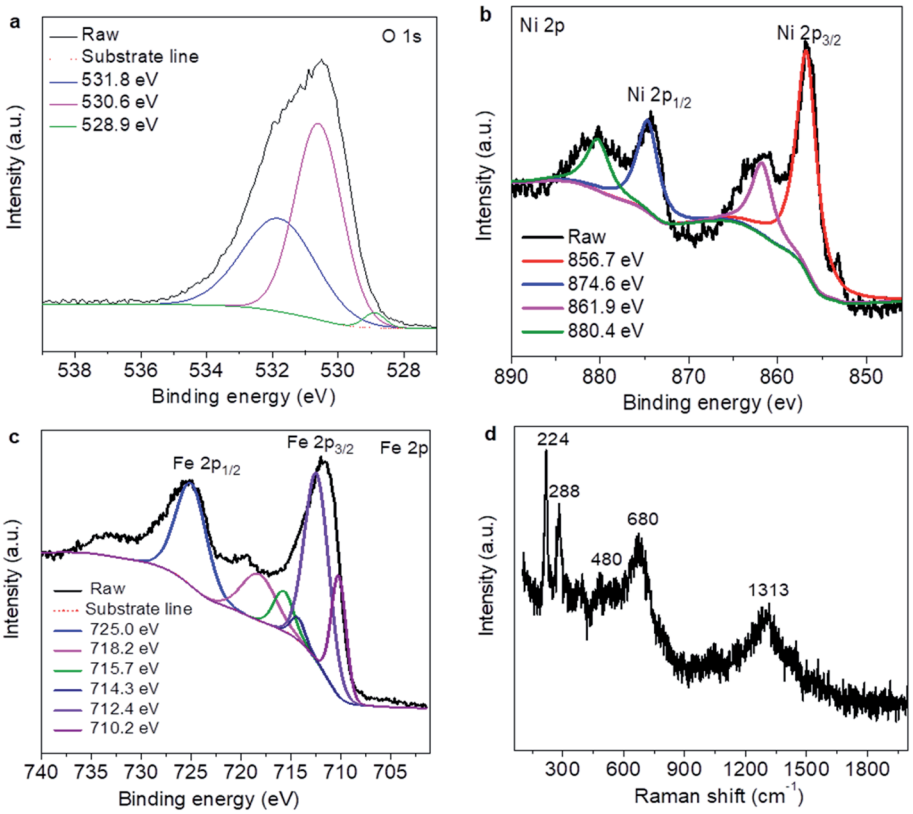

Fig. 3 XPS results of the NiFe(OH)$_X$ Nanoparticles/Ni foam sample (a–c) and Raman spectra of the NiFe(OH)$_X$ Nanoparticles/Ni foam sample (d).

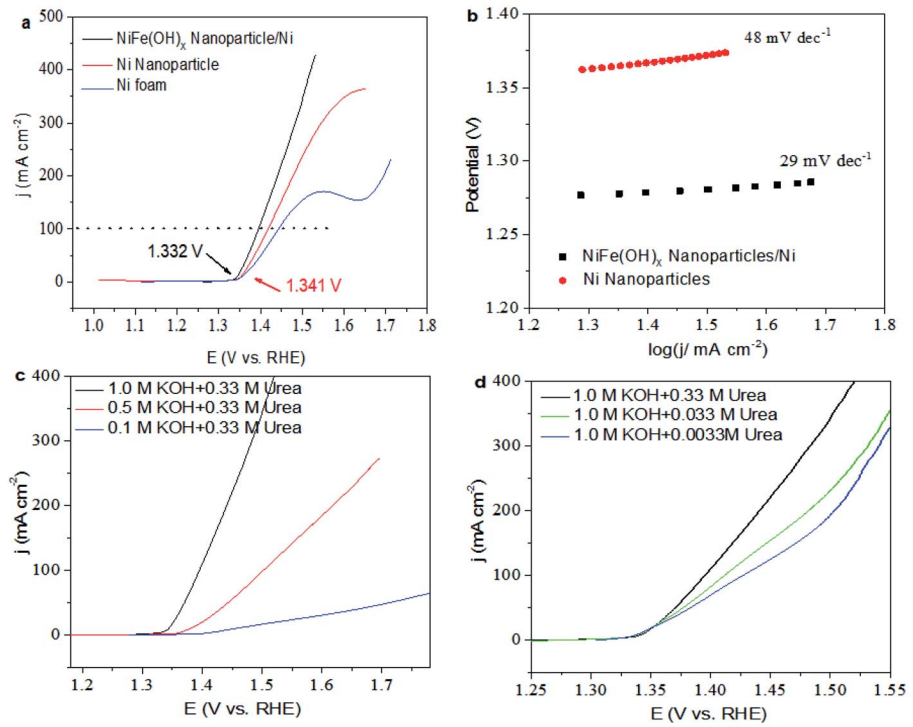

Fig. 4 (a) LSV curves of the NiFe(OH)$_X$ nanoparticles/Ni foam sample, the Ni/Ni foam and Ni foam in 1.0 M KOH electrolyte with 0.33 M urea at a scan rate of 10 mV s^{-1}. (b) Tafel plots of the NiFe(OH)$_X$ Nanoparticles/Ni foam sample and the Ni/Ni foam (c and d) LSV curves of different electrolyte and different urea concentration over the NiFe(OH)$_X$ nanoparticles/Ni foam sample.

nanoparticles/Ni foam sample was 29.0 mV dec^{-1}, which was much lower than that of the Ni/Ni foam (48.0 mV dec^{-1}), indicating its more outstanding kinetic for urea oxidation. Besides, the introduction of trivalent iron ions can also improve the active sites of the catalyst, thus greatly improving the catalytic performance. Compared with the electrocatalysts in the related UOR work reported previously (such as NF/NiMoO–Ar,[43] NiCo allay,[44] Ni graphene and Pt/C catalyst.[45]), the $NiFe(OH)_X$ nanoparticles/Ni foam sample exhibits higher activity. Of course, the electrolyte played a key role in catalyzing the UOR reaction. As the concentration of the electrolyte decreases, its catalytic activity will gradually decrease, thereby affecting the progress of the reaction in Fig. 4c. It was not difficult to find that when the concentration of urea decreases, the catalytic performance of the material would decrease. However, the effect of urea concentration is not as great as that of electrolyte concentration (Fig. 4d). Compared with OER reaction, urea oxidation has a higher level of significance: (a) the urea oxidation needs a remarkably lower thermodynamic cell voltage (0.37 V) than ordinary water electrolysis (1.23 V) under the standard conditions, (b) secondly, for the environmental pollution problem, it had guiding significance for effectively solving the excessive nitrogen compounds in sewage and preventing serious eutrophication of water bodies.[43] Therefore, the high-performance $NiFe(OH)_X$ nanoparticles/Ni foam is very important not only in the energy saving using it to catalyze UOR instead of OER for electrolytic hydrogen production, but also in the industrial wastewater treatment containing urea, urine treatment and so on.

Electrochemical active area (ECSA) is one of the important criteria to evaluate the excellence of catalysts, which is calculated by the capacitance of the electrochemical double-layer

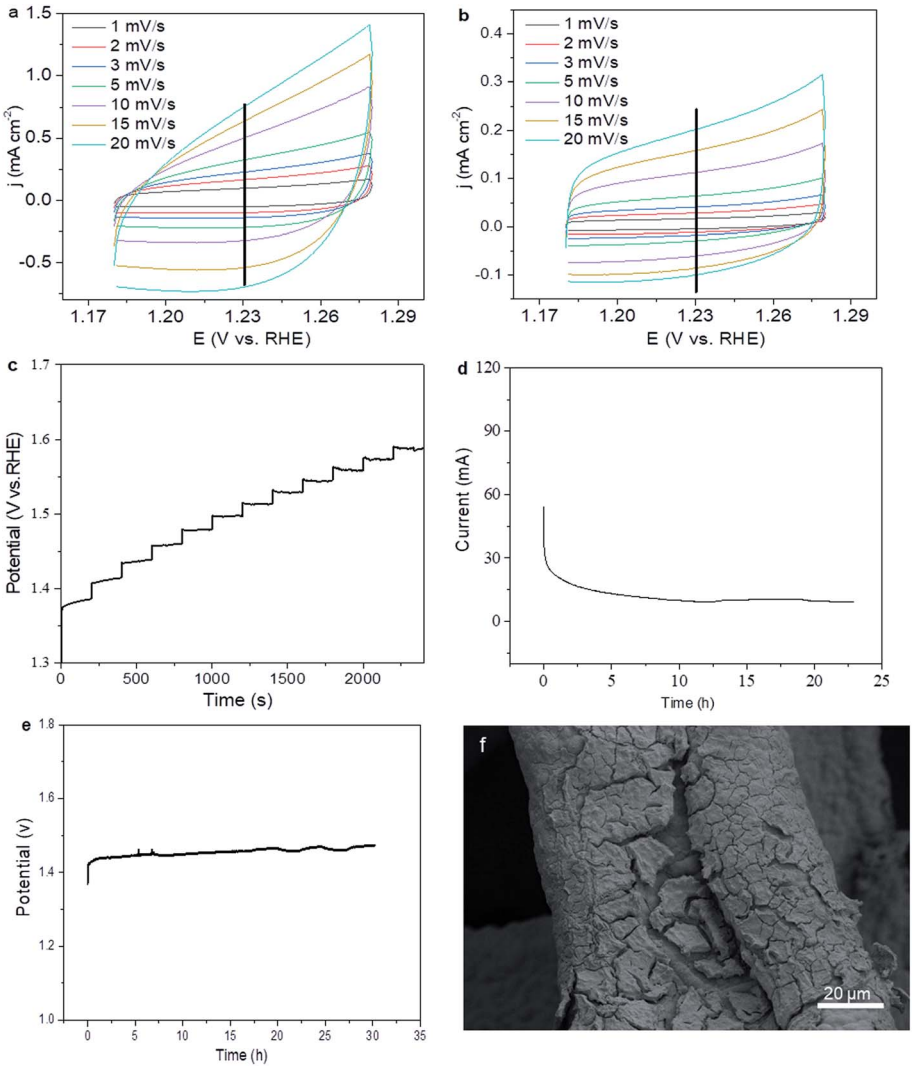

Fig. 5 CV curves at different scan rates in the non-faradaic capacitance current range for the $NiFe(OH)_X$ nanoparticles/Ni foam sample (a) and the Ni/Ni foam (b) in 1 M KOH electrolyte with 0.33 M urea. Chronopotentiometry curves of the $NiFe(OH)_X$ nanoparticles/Ni foam sample in 1 M KOH electrolyte with 0.33 M urea at various current densities (c). Galvanostatic experiment of the $NiFe(OH)_X$ nanoparticles/Ni foam sample for 23 h (d) and chronopotentiometry parameters of the $NiFe(OH)_X$ nanoparticles/Ni foam sample for 30 h under the condition of 50 mA cm^{-2} (e). (f) SEM image of the $NiFe(OH)_X$ nanoparticles/Ni foam for a long time test.

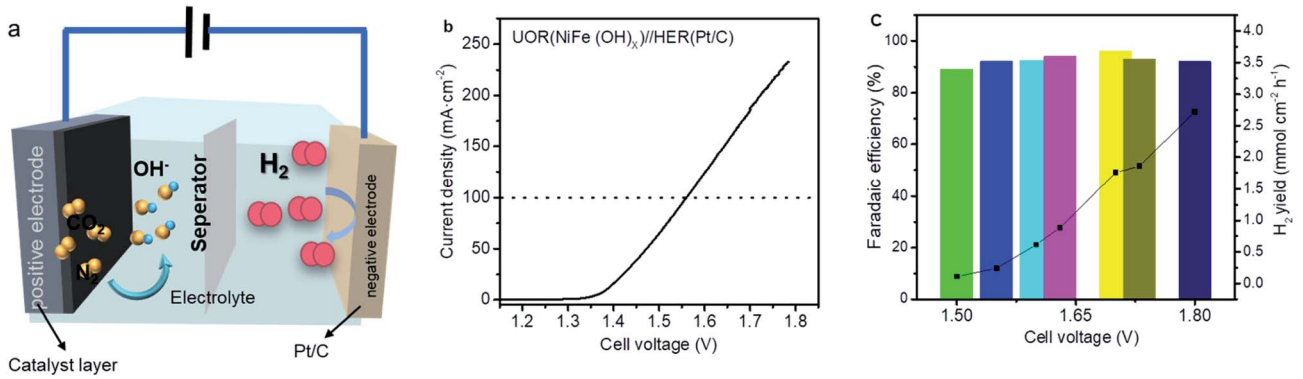

Fig. 6 (a) Schematic illustration of the two-electrode system in 1.0 M KOH electrolyte with 0.33 M urea. (b) LSV curves of the $NiFe(OH)_X$ nanoparticles/Ni foam sample in two-electrode system. (c) faradaic efficiency and yield of H_2 (mmol cm^{-2} h^{-1}).

(C_{dll}). As shown in Fig. 5a and b, the $NiFe(OH)_X$ nanoparticles/Ni foam sample in 1 M KOH electrolyte with 0.33 M urea was about 0.0668 F cm^{-2}, which was much higher than that of the Ni/Ni foam (0.01488 F cm^{-2}), indicating that the $NiFe(OH)_X$ nanoparticles/Ni foam sample had a larger ESCA. Fig. 5c showed that the chronopotentiometry curves of the $NiFe(OH)_X$ nanoparticles/Ni foam sample in 1 M KOH electrolyte with 0.33 M urea at various current densities, which was used to study the prolonged stability of the catalysts. It can be seen from Fig. 5c that the potential of each stage remains unchanged in the corresponding 200 seconds without *iR*-correction, which means that the electrode has excellent mass transfer characteristics, conductivity and mechanical stability.[12] As one of the key factors, the stability in Fig. 5d revealed that the chronopotentiometry curves of the $NiFe(OH)_X$ nanoparticles/Ni foam sample can steadily output with various current densities in 1 M KOH electrolyte with 0.33 M urea. Fig. 5d showed the galvanostatic experiment of the $NiFe(OH)_X$ nanoparticles/Ni foam sample for 23 h at the voltages of 1.368 V and chronopotentiometry parameters of the $NiFe(OH)_X$ nanoparticles/Ni foam sample for 30 h under the condition of 50 mA cm^{-2} was shown in Fig. 5e. The two life tests reveal that the electrocatalyst has good stability. Fig. 5f showed the SEM image of $NiFe(OH)_X$ nanoparticles/Ni foam for a long time test. From Fig. 1c and d and Fig. 5f, the $NiFe(OH)_X$ nanoparticles on the surface of nickel foam did not decrease and the structure did not collapse, indicating that the good stability of the electrocatalyst.

Fig. 6a shows the schematic illustration of the two-electrode system in 1.0 M KOH electrolyte with 0.33 M urea, in which the commercial Pt/C were used as the negative electrode. As shown in Fig. 6b, the $NiFe(OH)_X$ nanoparticles/Ni foam sample yield much greater UOR activity in two-electrode system with a lower potential of 1.56 V of achieving 100 mA cm^{-2}. The amount of hydrogen detected by gas chromatography was consistent with the theoretical value, equivalent to Faraday efficiency close to 100%. As illustrated in Fig. 6c, when the voltage of the two electrodes reaches 1.7 V, the Faraday efficiency of hydrogen was about 96%, which can produce hydrogen 1.7538 mmol cm^{-2} per hour, and its Faraday efficiency did not decrease with the increase of voltage.

4. Conclusions

In summary, we provided a rapid and large-scale preparation of three-dimensional nanostructure with the high active area, and suggested a new way to design and obtain high-performance electrocatalysts for UOR. The $NiFe(OH)_X$ nanoparticles/Ni foam sample had a larger ESCA. Compared to the most of UOR electrocatalysts reported, it exhibits higher activity and stability. In a two-electrode system only a low potential of 1.56 V was needed to drive the current density of 100 mA cm^{-2}. This work is very meaningful not only in the energy saving using the proposed electrocatalyst to catalyze UOR instead of OER for electrolytic hydrogen production, but also in the industrial wastewater treatment containing urea, urine treatment and so on.

Conflicts of interest

There are no conflicts of interest.

Acknowledgements

We acknowledge the funding support from National Natural Science Foundation of China (21771002), Open Fund for Discipline Construction (Institute of Physical Science and Information Technology, Anhui University).

References

1 S. Chu and A. Majumdar, *Nature*, 2012, **488**, 294–303.
2 B. Zhu, Z. Liang and R. Zou, *Small*, 2020, **16**, 1906133.
3 K. Ye, G. Wang, D. Cao and G. Wang, *Top. Curr. Chem.*, 2018, **376**, 42.
4 X. Sun and R. Ding, *Catal. Sci. Technol.*, 2020, **10**, 1567–1581.
5 J.-Y. Zhang, T. He, M. Wang, R. Qi, Y. Yan, Z. Dong, H. Liu, H. Wang and B. Y. Xia, *Nano Energy*, 2019, **60**, 894–902.
6 C. B. Sun, M. W. Guo, S. S. Siwal and Q. B. Zhang, *J. Catal.*, 2020, **381**, 454–461.
7 S. Cobo, J. Heidkamp, P.-A. Jacques, J. Fize, V. Fourmond, L. Guetaz, B. Jousselme, V. Ivanova, H. Dau, S. Palacin, M. Fontecave and V. Artero, *Nat. Mater.*, 2012, **11**, 802–807.

8 A. Majeed, X. Li, P.-X. Hou, H. Tabassum, L. Zhang, C. Liu and H.-M. Cheng, *Appl. Catal., B*, 2020, **269**, 118823.
9 C. Wang, X. Shao, J. Pan, J. Hu and X. Xu, *Appl. Catal., B*, 2020, **268**, 118435.
10 D. Zhu, L. Wang, M. Qiao and J. Liu, *Chem. Commun.*, 2020, **56**, 7159–7162.
11 Y. Li, X. Wei, L. Chen, J. Shi and M. He, *Nat. Commun.*, 2019, **10**, 5335.
12 X. Xu, P. Du, T. Guo, B. Zhao, H. Wang and M. Huang, *ACS Sustainable Chem. Eng.*, 2020, **8**, 7463–7471.
13 Y. Wang, Y. Li, L. Ding and J. Ding, *Chem. Commun.*, 2019, **55**, 13562–13565.
14 S. Adhikari, Y. Kwon and D.-H. Kim, *Chem. Eng. J.*, 2020, **402**, 126192.
15 M. Song, Z. Zhang, Q. Li, W. Jin, Z. Wu, G. Fu and X. Liu, *J. Mater. Chem. A*, 2019, **7**, 3697–3703.
16 M. Zeng, J. Wu, Z. Li, H. Wu, J. Wang, H. Wang, L. He and X. Yang, *ACS Sustainable Chem. Eng.*, 2019, **7**, 4777–4783.
17 J. Zhang, F. Xing, H. Zhang and Y. Huang, *Dalton Trans.*, 2020, **49**, 13962–13969.
18 G. Das, R. M. Tesfaye, Y. Won and H. H. Yoon, *Electrochim. Acta*, 2017, **237**, 171–176.
19 W. Xu, D. Du, R. Lan, J. Humphreys, Z. Wu and S. Tao, *New J. Chem.*, 2017, **41**, 4190–4196.
20 Z. Wang, W. Liu, Y. Hu, M. Guan, L. Xu, H. Li, J. Bao and H. Li, *Appl. Catal., B*, 2020, **272**, 118959.
21 H. M. Abd El-Lateef, M. M. Khalaf, M. A. Al-Omair, V.-D. Dao and I. M. A. Mohamed, *Mater. Lett.*, 2020, **276**, 128192.
22 G. Ma, Q. Xue, J. Zhu, X. Zhang, X. Wang, H. Yao, G. Zhou and Y. Chen, *Appl. Catal., B*, 2020, **265**, 118567.
23 E. T. Sayed, T. Eisa, H. O. Mohamed, M. A. Abdelkareem, A. Allagui, H. Alawadhi and K.-J. Chae, *J. Power Sources*, 2019, **417**, 159–175.
24 Z. Feng, D. Li, L. Wang, Q. Sun, P. Lu, P. Xing and M. An, *Electrochim. Acta*, 2019, **304**, 275–281.
25 H. Hosseini and S. Shahrokhian, *Chem. Eng. J.*, 2019, **375**, 122090.
26 P. Babar, A. Lokhande, V. Karade, I. J. Lee, D. Lee, S. Pawar and J. H. Kim, *J. Colloid Interface Sci.*, 2019, **557**, 10–17.
27 Q. Gan, X. Cheng, J. Chen, D. Wang, B. Wang, J. Tian, T. T. Isimjan and X. Yang, *Electrochim. Acta*, 2019, **301**, 47–54.
28 L. Xia, Y. Liao, Y. Qing, H. Xu, Z. Gao, W. Li and Y. Wu, *ACS Appl. Energy Mater.*, 2020, **3**, 2996–3004.
29 W.-K. Han, X.-P. Li, L.-N. Lu, T. Ouyang, K. Xiao and Z.-Q. Liu, *Chem. Commun.*, 2020, **56**, 11038–11041.
30 C. Li, Y. Liu, Z. Zhuo, H. Ju, D. Li, Y. Guo, X. Wu, H. Li and T. Zhai, *Adv. Energy Mater.*, 2018, **8**, 1801775.
31 P. Salarizadeh, M. B. Askari, N. Askari and N. Salarizadeh, *Mater. Chem. Phys.*, 2020, **239**, 121958.
32 Z. Wu, X. Guo, Z. Zhang, M. Song, T. Jiao, Y. Zhu, J. Wang and X. Liu, *ACS Sustainable Chem. Eng.*, 2019, **7**, 16577–16584.
33 D. Zhu, C. Guo, J. Liu, W. Liang, D. Yi and S. Z. Qiao, *Chem. Commun.*, 2017, **53**, 10906–10909.
34 D. Zhu, M. Qiao, J. Liu, T. Tao and C. Guo, *J. Mater. Chem. A*, 2020, **8**, 8143–8170.
35 Z. W. Seh, J. Kibsgaard, C. F. Dickens, I. Chorkendorff, J. K. Nørskov and T. F. Jaramillo, *Science*, 2017, **355**, eaad4998.
36 D. Voiry, R. Fullon, J. Yang, C. de Carvalho Castro e Silva, R. Kappera, I. Bozkurt, D. Kaplan, M. J. Lagos, P. E. Batson, G. Gupta, A. D. Mohite, L. Dong, D. Er, V. B. Shenoy, T. Asefa and M. Chhowalla, *Nat. Mater.*, 2016, **15**, 1003–1009.
37 M.-S. Wu, Y.-J. Sie and S.-B. Yang, *Electrochim. Acta*, 2019, **304**, 131–137.
38 Q. Jia, X. Wang, S. Wei, C. Zhou, J. Wang and J. Liu, *Appl. Surf. Sci.*, 2019, **484**, 1052–1060.
39 Z.-Y. Wu, P. Chen, Q.-S. Wu, L.-F. Yang, Z. Pan and Q. Wang, *Nano Energy*, 2014, **8**, 118–125.
40 W. Genxiang and W. Zhenhai, *Nanoscale*, 2018, **10**, 2108–21095.
41 H. Yang, C. Wang, Y. Zhang and Q. Wang, *Sci. China Mater.*, 2018, **62**, 681–689.
42 C. Liang, P. Zou, A. Nairan, Y. Zhang, J. Liu, K. Liu, S. Hu, F. Kang, H. J. Fan and C. Yang, *Energy Environ. Sci.*, 2020, **13**, 86–95.
43 Z.-Y. Yu, C.-C. Lang, M.-R. Gao, Y. Chen, Q.-Q. Fu, Y. Duan and S.-H. Yu, *Energy Environ. Sci.*, 2018, **11**, 1890–1897.
44 W. Xu, H. Zhang, G. Li and Z. Wu, *Sci. Rep.*, 2014, **4**, 5863.
45 D. Wang, W. Yan, S. H. Vijapur and G. G. Botte, *Electrochim. Acta*, 2013, **89**, 732–736.